LANGMUIR

pH-Modulated Nanoarchitectonics for Enhancement of Multivalency-Induced Vesicle Shape Deformation at Receptor-Presenting Lipid Membrane Interfaces

Hyeonjin Park, Tun Naw Sut, Abdul Rahim Ferhan, Bo Kyeong Yoon, Vladimir P. Zhdanov, Nam-Joon Cho,* and Joshua A. Jackman*

Read Online

ACCESS | Metrics & More | Article Recommendations | Supporting Information

ABSTRACT: Multivalent ligand−receptor interactions between receptor-presenting lipid membranes and ligand-modified biological and biomimetic nanoparticles influence cellular entry and fusion processes. Environmental pH changes can drive these membrane-related interactions by affecting membrane nanomechanical properties. Quantitatively, however, the corresponding effects on high-curvature, sub-100 nm lipid vesicles are scarcely understood, especially in the multivalent binding context. Herein, we employed the label-free localized surface plasmon resonance (LSPR) sensing technique to track the multivalent attachment kinetics, shape deformation, and surface coverage of biotin ligand-functionalized, zwitterionic lipid vesicles with different ligand densities on a streptavidin receptor-coated supported lipid bilayer under varying pH conditions (4.5, 6, 7.5). Our results demonstrate that more extensive multivalent interactions caused greater vesicle shape deformation across the tested pH conditions, which affected vesicle surface packing as well. Notably, there were also pH-specific differences, i.e., a higher degree of vesicle shape deformation was triggered at a lower multivalent binding energy in pH 4.5 than in pH 6 and 7.5 conditions. These findings support that the nanomechanical properties of high-curvature lipid membranes, especially the membrane bending energy and the corresponding responsiveness to multivalent binding interactions, are sensitive to solution pH, and indicate that multivalency-induced vesicle shape deformation occurs slightly more readily in acidic pH conditions relevant to biological environments.
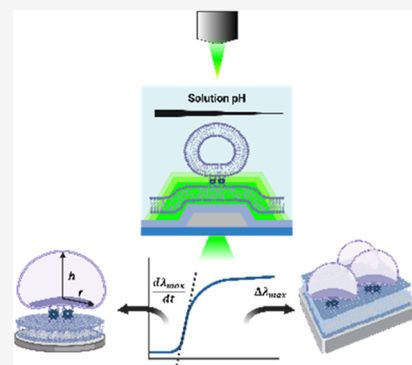
INTRODUCTION

The engagement of multiple ligand−receptor bonds, so-called multivalent binding interactions, is associated with a variety of biomacromolecular interaction processes that occur at the interface between cell membranes and biological nanoparticles such as extracellular vesicles[1] and virions[2,3] along with biomimetic drug and vaccine delivery carriers such as lipid nanoparticles (LNPs).[4] For example, exosome binding to cell membranes plays an important role in regulating cell-to-cell communication and cancer cell proliferation,[5] and receptor-mediated binding is critical to cellular internalization by virions and resulting infectivity processes.[6] In the field of LNP-based delivery vehicles, receptor-mediated endocytosis and subsequent internalization through cell membranes have been proposed as a mechanism for cellular uptake,[7] and thus understanding the interplay between multivalency and the nanomechanical properties of LNPs can help to rationalize the mechanism of their internalization process. Therefore, researchers have focused on investigating the nanomechanical properties of membrane-enveloped LNPs via ligand−receptor binding interactions by various experimental techniques such as fluorescence microscopy,[8,9] quartz crystal microbalance-dissipation (QCM-D),[10] and surface plasmon resonance

(SPR).[11] Understanding the effect of environmental pH on these properties is a central issue in the field.[12]

Since planar-supported lipid bilayers (SLBs) and nanoscopic lipid vesicles can be readily prepared and tuned by varying preparation conditions, such nanoarchitectures have been extensively utilized in most of the relevant biophysical studies as simple models of the cell membrane and LNPs/extracellular vesicles, respectively.[13,14] Early work focused on developing a measurement platform to monitor the attachment of biotin-modified lipid vesicles onto a streptavidin-coated SLB surface and resulting vesicle shape deformation in multivalent ligand−receptor interaction contexts.[15] More recently, this measurement approach has gained scientific interest to study various factors that influence the membrane properties of LNPs such as nanoparticle size,[16,17] lipid composition,[18,19] and cholesterol fraction,[20] which indicates the potential to further assess the

A

effect of environmental conditions, including salt[21] and solution pH.[22]

In biological systems, LNP-based delivery vehicles encounter aqueous environments with different pH levels,[23,24] which can range from the extracellular environment around pH 7.4 to mature endosomal interiors that can drop to below pH 5.[25] This pH variation is the basis for designing ionizable lipids while the fundamental properties of conventionally used zwitterionic phospholipids—employed in LNPs as helper lipids and more broadly in lipid-based nanoparticles as the main component—are also affected by these pH changes. In particular, the effect of pH on the stability of individual LNPs containing ionizable lipids and contacting an SLB has recently been scrutinized.[12] In a broader context, the membrane bending rigidity—a quantitative parameter to describe the intrinsic nanomechanical properties of lipid bilayers—has also been examined for zwitterionic phosphatidylcholine (PC) membrane models and shown to exhibit modest pH-dependent variations in giant unilamellar vesicle (GUV) and in small unilamellar vesicle (SUV) systems.[26,27] Other studies have demonstrated that the interfacial tension, membrane dipole potential, and lipid mobility of zwitterionic lipid bilayers can also be affected by solution pH conditions.[28,29] Additionally, it has been demonstrated that changes in solution pH can affect the membrane fusion process between two planar PC lipid bilayer membranes,[30] supporting that such biological processes are related to fundamental membrane properties. While it is widely understood that solution pH affects the intrinsic nanomechanical properties of zwitterionic lipid bilayers, it remains to be clarified how such variations may influence multivalent binding interactions involving ligand-modified vesicles, especially considering that sub-100 nm lipid vesicles can have appreciably higher membrane bending rigidities than flatter membranes.[17]

To address this question, herein, we employed the localized surface plasmon resonance (LSPR) sensing technique to scrutinize the multivalent binding interactions between biotin-modified, sub-100 nm lipid vesicles and streptavidin-coated SLB platforms in different pH conditions, i.e., pH 4.5, 6, and 7.5, that reflect the range of typical extracellular, cytosolic, and specific organelle conditions encountered in biological systems (as reviewed in ref 25). By systematically tuning the biotinylated lipid ligand fraction in the vesicles from 0.25 to 1 mol %, we were also able to modulate the multivalent biotin—streptavidin binding interaction energy whereby a larger ligand fraction corresponds to a greater multivalent binding interaction energy. This biomimetic platform approach, including analytical modeling of the LSPR measurement response as employed earlier[15,17] to tackle other aspects of the system under consideration, enabled us to obtain fundamental insights into how environmental pH condition affects multivalency-induced vesicle adsorption and resulting shape deformation of attached vesicles. Furthermore, based on the analytical modeling, we could also extract quantitative information about the surface coverage of attached vesicles and evaluate how multivalency-induced shape deformation influences the corresponding jamming limit.

■ MATERIALS AND METHODS

Materials. 1,2-Dioleoyl-*sn*-glycero-3-phosphocholine (DOPC, pK_a of its phosphate group is ~1; ref 31), 1,2-dihexanoyl-*sn*-glycero-3-phosphocholine (DHPC), and 1,2-dioleoyl-*sn*-glycero-3-phosphoethanolamine-*N*-(cap biotinyl) (DOPE-Biotin) lipids in chloroform

were purchased from Avanti Polar Lipids (Alabaster, AL). Lyophilized streptavidin (catalog no. S203) was acquired from Leinco (St. Louis, MO) and other reagents were obtained from Sigma-Aldrich (St. Louis, MO). Aqueous buffer solutions composed of 10 mM Tris and 150 mM NaCl were prepared using deionized water (>18 MΩ·cm) that was obtained from a Milli-Q water purification system (MilliporeSigma, Burlington, MA). The solution pH was adjusted by adding HCl and NaOH as appropriate until reaching the desired pH value.

Sample Preparation. Bicelles, employed to fabricate an SLB on the sensor surface, were generated by using a mixture of DOPC, DOPE-Biotin, and DHPC lipids based on the freeze−thaw−vortex cycling method.[32] The concentrations of long- and short-chain lipids were fixed at 1 and 4 mM, respectively, and accordingly, the *q*-ratio ([DOPC + DOPE-Biotin]/[DHPC]) was 0.25, whereas the DOPE-Biotin fraction in the [DOPC + DOPE-Biotin] concentration used for SLB preparation was fixed at 1 mol %. Of note, long-chain phospholipids self-assemble to form an SLB on the sensor surface while short-chain lipids leave the surface and are washed away during the buffer washing step.[33] For vesicle fabrication, DOPC and DOPE-Biotin lipids were mixed at the appropriate molar ratios while the total mass concentration was kept at 5 mg/mL, followed by extrusion using 50 nm diameter polycarbonate membranes, as previously described.[34] The molar ratio of DOPE-Biotin lipids in the vesicles ranged from 0.25 to 1 mol % and the diameters of the resulting vesicles were determined to be around 75 nm by dynamic light scattering (DLS) measurements. Before experiment, the stock solutions of bicelles and vesicles were diluted by around 32 and 50 times in Tris buffer with appropriate pH values. Lyophilized streptavidin was solubilized at a concentration of 24 μM in Milli-Q-treated water and, before experiment, the streptavidin protein sample was diluted with Tris buffer solution to a concentration of 1 μM, which is a sufficiently high concentration to ensure that the biotinylated SLB surface with 1 mol % DOPE-Biotin lipid is fully saturated with attached streptavidin molecules.[35]

LSPR Measurements. The experiments were performed on silica-coated silver nanodisk arrays by using an Insplorion XNano instrument (Insplorion AB, Gothenburg, Sweden). To prepare silica-coated silver sensor chips, silver nanodisks were deposited on a glass substrate by hole-mask colloidal lithography,[36] followed by sputter-coating a thin silicon nitride overlayer across the entire surface.[37] Prior to each experiment, the sensor chips were rinsed with ethanol and dried under a nitrogen gas flow, followed by treatment with oxygen plasma (PDC-002, Harrick Plasma, Ithaca, NY) at 180 W for 1 min. After this cleaning step, the sensor chip was assembled within the measurement chamber, followed by the introduction of liquid sample at a constant flow rate of 50 μL/min by using a peristaltic pump (Reglo Digital, Ismatec, Glattbrugg, Switzerland). Transmission-mode optical extinction spectra were measured by a UV−visible spectrophotometer, and the centroid position in the spectrum was defined as the LSPR peak wavelength (λ_{max}).[38] All measurement data were collected every 1 s by the Insplorer software package (Insplorion AB). In applicable cases, statistical analysis of measurement data between multiple test groups was conducted by one-way analysis of variance (ANOVA) with Tukey's multiple comparison test in the GraphPad Prism8 software (GraphPad Software, San Diego, CA), and multiplicity-adjusted *P* values of 0.05 were considered statistically significant.

■ RESULTS AND DISCUSSION

Nanoplasmonic Sensing Strategy. Figure 1A schematically illustrates the LSPR-based measurement platform that was fabricated on the silica-coated sensor surface by sequential exposure to (i) biotinylated lipid bicelles, (ii) streptavidin protein, and (iii) biotinylated lipid vesicles. To investigate how environmental pH conditions affect multivalency-related vesicle attachment, we systematically tuned the solution pH across the range of 4.5−7.5 while the biotinylated lipid fraction
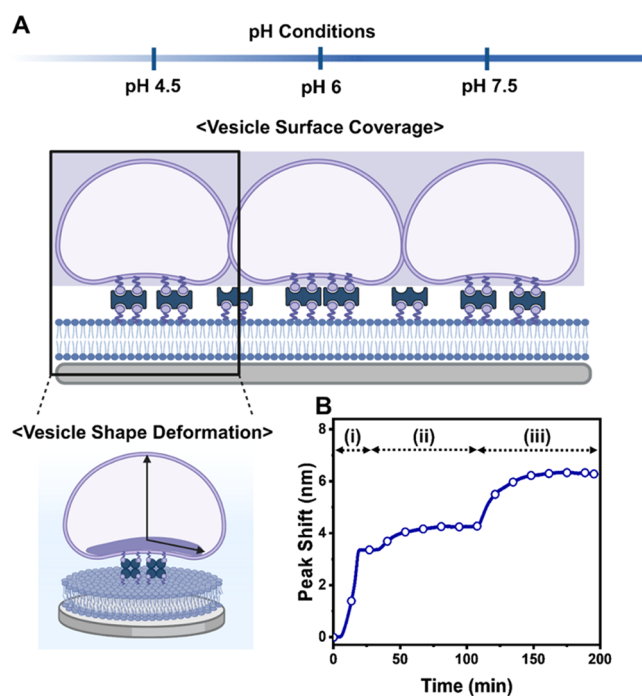
Figure 1. LSPR measurement strategy to track pH-induced changes in multivalent binding interactions of sub-100 nm lipid vesicles. (A) Schematic illustration of LSPR measurement platform composed of (i) biotinylated SLB, (ii) streptavidin protein, and (iii) sub-100 nm, biotinylated lipid vesicle adlayers under various pH conditions (4.5, 6, 7.5). Analytical modeling of the LSPR measurement response can extract quantitative information about the shape deformation of attached vesicles at low surface coverage and adlayer properties at saturation coverage. (B) Time-resolved LSPR $\Delta\lambda_{max}$ shift response for a representative experimental protocol on a silica-coated silver nanodisk array. The experimental steps included (i) addition of biotinylated lipid bicelles to promote SLB formation, (ii) addition of streptavidin protein molecules to functionalize the SLB surface, and (iii) addition of biotinylated lipid vesicles that can selectively bind to the streptavidin-coated SLB platform. Steps (i, ii) were conducted at pH 7.5 and the solution pH was then exchanged to the appropriate pH value before conducting step (iii).

in the vesicles was varied from 0.25 to 1 mol %. The time-resolved $\Delta\lambda_{max}$ shift was tracked throughout the measurements and a positive $\Delta\lambda_{max}$ shift resulting from vesicle addition to the SLB platform corresponds to an increase in the local refractive index near the sensor surface due to either increased vesicle mass attachment and/or greater deformation of attached vesicles, whereby the lipid mass in an attached vesicle lies closer, on average, to the sensor surface.[39,40] Analytical modeling of the LSPR measurement response and corresponding optical adlayer properties allowed us to extract quantitative information about how multivalent binding interactions influenced vesicle shape deformation (by using the approach described in detail earlier in refs 15 and 17; see also Section 1 in the Supporting Information) and surface coverage of attached vesicles (Section 2 in the Supporting Information), including the relationship between these two factors.

A representative LSPR sensorgram of the experimental protocol is presented in Figure 1B, which consists of the following steps: (i) an initial baseline was recorded in Tris buffer (pH 7.5) and then a bicelle-containing solution was added to fabricate the biotinylated SLB on the sensor surface, followed by a buffer washing step; (ii) the SLB surface was

functionalized with streptavidin protein receptors and then washed with the same buffer solution; and (iii) the buffer solution was next exchanged with another buffer solution at the desired pH, followed by biotinylated lipid vesicle addition and a washing step with equivalent buffer solution. The fabricated SLB platform contained 1 mol % biotinylated lipid in all cases so that the corresponding amount of bound streptavidin protein molecules was consistent, which was verified by the $\Delta\lambda_{max}$ shift recorded during that step (Figure S1).

LSPR Measurements. Representative time-resolved $\Delta\lambda_{max}$ shift responses for biotinylated lipid vesicle attachment onto streptavidin-modified SLB platforms are presented in Figure 2A–C. The molar fraction of biotinylated lipid in the vesicles was systematically tuned from 0.25 to 1 mol % and vesicle addition was performed in different pH conditions that ranged from pH 4.5 to 7.5. At all tested pH conditions, monotonic adsorption kinetics until reaching saturation were observed and the $\Delta\lambda_{max}$ shift at saturation tended to be greater at higher biotinylated lipid fractions in the vesicles. The corresponding LSPR measurement responses measured at each tested pH condition are summarized in Figure 2D. Vesicle attachment at pH 7.5 yielded final $\Delta\lambda_{max}$ shifts around 1.58 ± 0.06, 2.00 ± 0.02, and 2.03 ± 0.04 nm when the biotinylated lipid fractions in the vesicles were 0.25, 0.5, and 1 mol %, respectively. Similar measurement responses were observed for vesicle attachment at pH 6, with corresponding final $\Delta\lambda_{max}$ shifts around 1.63 ± 0.07, 1.97 ± 0.02, and 2.06 ± 0.07 nm. In addition, for vesicle attachment at pH 4.5, the final $\Delta\lambda_{max}$ shifts were also around 1.72 ± 0.01, 2.08 ± 0.01, and 2.06 ± 0.04 nm for vesicles with 0.25, 0.5, and 1 mol % biotinylated lipid fractions, respectively. Thus, the dependence of the $\Delta\lambda_{max}$ shifts at saturation on the ligand density was similar across all tested pH conditions.

Next, we evaluated the initial rate of change in the time-resolved $\Delta\lambda_{max}$ signal during vesicle attachment in the low surface coverage regime, which provides insight into the relative extent of multivalency-induced shape deformation of attached vesicles (Figure 3). Since the vesicle attachment rate is controlled by diffusion and the bulk concentration of vesicles was fixed, the LSPR signal is sensitive to the shape of attaching vesicles whereby a larger rate indicates greater shape deformation.[15,17] In general, a greater density of multivalent biotin–streptavidin binding interactions at higher ligand densities drove more extensive vesicle shape deformation across the tested pH conditions, but there were also important differences depending on the solution pH. For vesicle attachment at pH 7.5, the rates were 0.33 ± 0.01 nm/min in the case of 0.25 mol % biotinylated vesicles, while the slope increased to 0.36 ± 0.01 and 0.43 ± 0.01 nm/min for 0.5 and 1 mol % biotinylated lipid vesicles, respectively (Figure 3A). A similar rate trend was observed at pH 6, and the corresponding rates were 0.38 ± 0.02, 0.39 ± 0.02, and 0.46 ± 0.03 nm/min for the 0.25, 0.5, and 1 mol % biotinylated vesicle cases, respectively (Figure 3B). In the latter two pH conditions, the key transition point in the rate change occurred when the biotinylated lipid fraction was changed from 0.5 to 1 mol %.

On the other hand, for pH 4.5, the rates were 0.36 ± 0.03, 0.43 ± 0.01, and 0.41 ± 0.03 nm/min for the 0.25, 0.5, and 1 mol % biotinylated vesicle cases, respectively (Figure 3C). Hence, the most pronounced rate change in this case occurred when the biotinylated lipid fraction changed from 0.25 to 0.5 mol %, supporting that the multivalent biotin–streptavidin energy was counterposed by a weaker membrane bending energy at pH 4.5 than at pH 6 or 7.5. Indeed, the measured
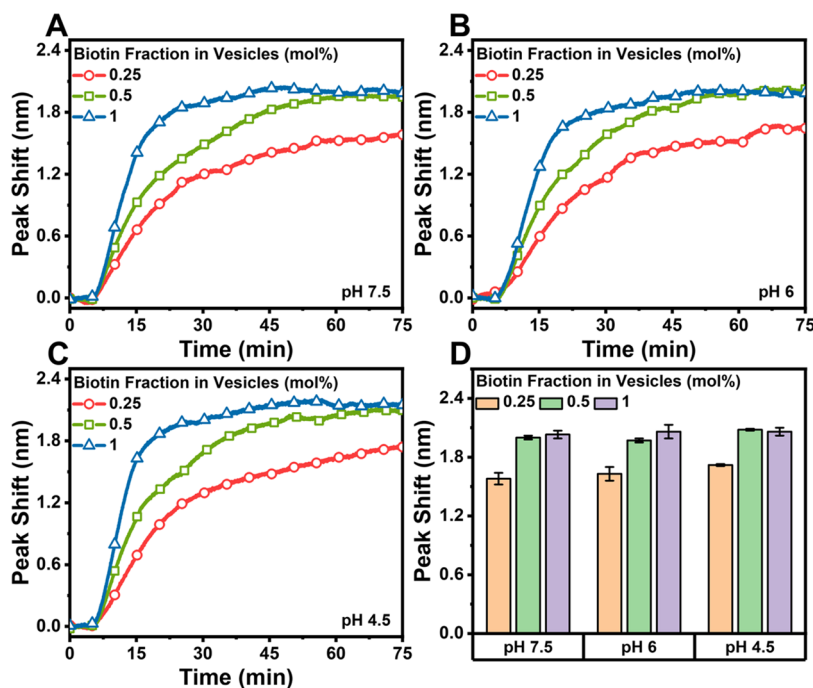
Figure 2. LSPR tracking of biotinylated lipid vesicle addition to streptavidin-coated SLB platforms in different pH conditions. (A−C) Time-resolved LSPR $\Delta\lambda_{max}$ shift responses for the vesicle attachment step in different pH conditions as a function of biotinylated lipid fraction in the vesicles. The baseline values correspond to a fabricated streptavidin-bound SLB platform in the appropriate pH conditions. Vesicle addition started from t = 5 min and a buffer washing step commenced from t = 65 min. (D) Summary of the corresponding final $\Delta\lambda_{max}$ shifts for vesicle attachment at saturation across all tested pH conditions. For panel (D), the measurement values are presented as the mean ± standard deviation from n = 3 experiments.
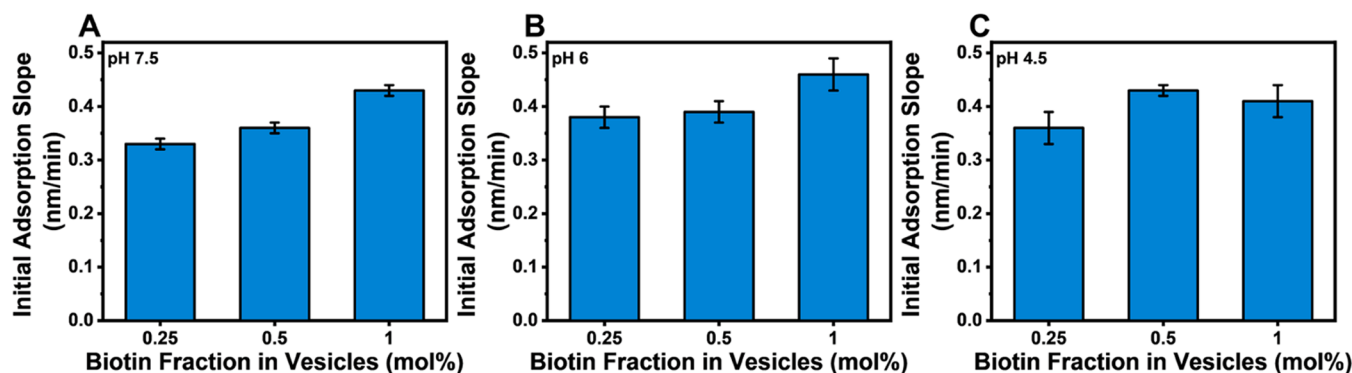
Figure 3. Effect of solution pH on the initial rate of LSPR-tracked vesicle attachment to SLB platform. (A−C) Rates of change in the time-resolved $\Delta\lambda_{max}$ signals corresponding to the initial vesicle attachment stage in the pH 7.5, 6, and 4.5 conditions. Using linear regression analysis, the values were extracted from the LSPR measurement data in Figure 2. All measurement values are presented as the mean ± standard deviation from n = 3 experiments.

rates at 0.5 mol % fraction in the pH 4.5 case already reached the maximum rate, i.e., the multivalent binding energy in that condition was already sufficient to maximally deform attached vesicles. In marked contrast, the measured rates at 0.5 mol % fraction in the other pH cases were appreciably smaller than the maximum rates that occurred at 1 mol % fraction ($P <$ 0.05, one-way ANOVA). Together, these findings demonstrate that attached vesicles in pH 4.5 are more sensitive to multivalency-induced shape deformation at a relatively lower ligand density and lead us to further quantify the pH-related variations in shape deformation effects.

Structural Analysis of Vesicle Deformation. In our analytical modeling approach (Figure 4A, and Sections 1 and 2 in the Supporting Information), an attached vesicle is viewed

as a truncated sphere of radius R_v (in the nondeformed state, the radius is designated to be R) with contact radius, r, contact area, $A = \pi r^2$, and height, h. In this framework, the contribution of a vesicle to the LSPR signal depends on the extent of multivalency-induced vesicle deformation (whereby greater deformation induces the lipid mass in an attached vesicle to lie closer to the sensor surface) and mathematically is proportional to $2aR_v + r^2$, where a = 14 nm is the LSPR-related penetration depth.[17] More specifically, the LSPR signal can be represented as

$$\Delta\lambda_{max} = G(2aR_v + r^2)C_a \tag{1}$$

where G is a constant that depends on the sensor sensitivity, optical properties of lipids and the bulk solution, and lipid
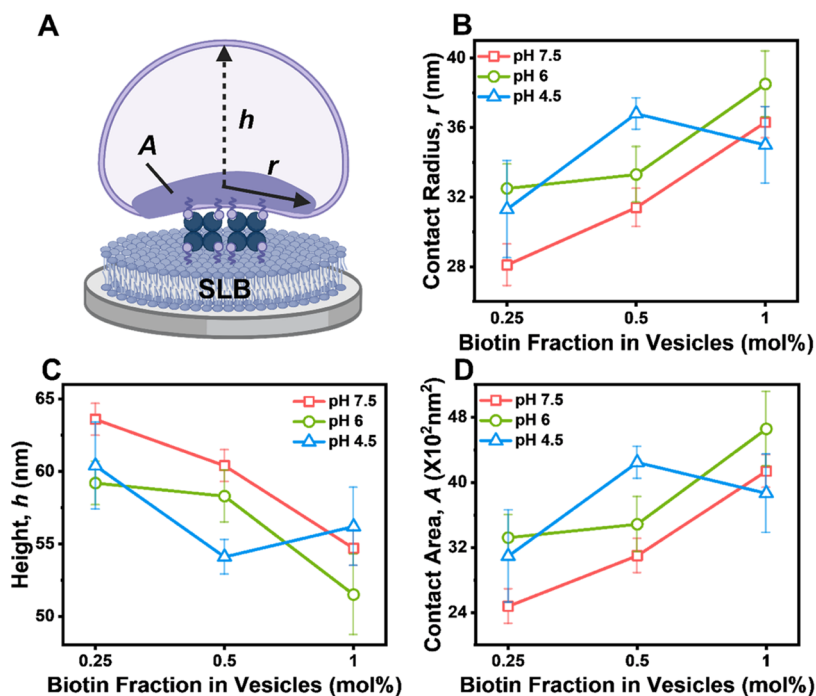
Figure 4. Structural analysis of attached vesicle deformation from LSPR measurement responses. (A) Vesicle model in the deformed state, as a truncated sphere with contact radius, r, contact area, $A = \pi r^2$, and height, h. (B) Truncation radius, r, characterizing the contacts with streptavidin-functionalized SLB surface, as a function of mol % of biotin ligands in the vesicles for each pH condition. (C) Height of a vesicle in the deformed state, h, and (D) the corresponding area of vesicle−SLB contact region, A, as a function of mol % of biotin ligands in the vesicles under the various pH conditions. All measurement values are represented as mean $\pm$ standard deviation from $n = 3$ experiments.

bilayer thickness, and C_a is the surface concentration of attached vesicles.

Since G can be calculated, eq 1 can be used to quantify the vesicle geometry (R_v and r) provided C_a is known, or C_a provided the geometry is known. During the initial (linear) phase of the attachment kinetics, as already noticed, the vesicle uptake is controlled by diffusion, C_a can be calculated [see eq 7 in the Supporting Information of ref 17], and accordingly, we can quantify the vesicle geometry.

Figure 4B presents the radius of the vesicle region that contacts the SLB surface in different pH conditions as a function of biotinylated lipid fraction in the vesicles. At pH 7.5, the contact radius of 0.25 mol % biotinylated lipid vesicles was 28.1 $\pm$ 1.2 nm, and the value increased to 31.4 $\pm$ 1.1 and 36.3 $\pm$ 0.9 nm for 0.5 and 1 mol % biotinylated lipid vesicles, respectively. This trend corresponds to around ~12 and ~29% increases in contact radius at 0.5 and 1 mol % biotin fractions, respectively, compared to the 0.25 mol % fraction. At pH 6, the contact radius was 32.5 $\pm$ 1.4 and 33.3 $\pm$ 1.6 nm for 0.25 and 0.5 mol % biotinylated lipid vesicles, respectively, while the corresponding value increased to 38.5 $\pm$ 1.9 nm for vesicles with 1 mol % biotinylated lipid fraction. This trend corresponds to around ~2 and ~18% increases in contact radius at 0.5 and 1 mol % biotin fractions, respectively, compared to the 0.25 mol % fraction. On the other hand, at pH 4.5, the contact radius was 31.3 $\pm$ 2.8, 36.8 $\pm$ 0.9, and 35.0 $\pm$ 2.2 nm for vesicles with 0.25, 0.5, and 1 mol % biotinylated lipid fractions, respectively. This trend corresponds to around ~18 and ~12% increases in contact radius at 0.5 and 1 mol % biotin fractions, respectively, compared to the 0.25 mol % fraction. Hence, a general tendency for attached vesicles to undergo greater extensive shape deformation at higher biotin fractions occurred for all tested pH conditions, while the onset

of peak deformation was already reached at 0.5 mol % biotin fraction for the pH 4.5 case and peak deformation levels did not occur until 1 mol % biotin fraction for the pH 6 and 7.5 cases.

Taking into account the relationship between the radius, R_v, and basement radius, r, of a deformed vesicle, we also calculated the height of attached vesicles on the SLB surface (Figure 4C). At pH 7.5, the height was 63.6 $\pm$ 1.1 nm in the case of 0.25 mol % biotinylated lipid vesicle, and decreased to around 60.4 $\pm$ 1.1 for 0.5 mol % biotinylated lipid vesicles and 54.7 $\pm$ 1.2 nm for 1 mol % biotinylated lipid vesicles. At pH 6, the height of the 0.25 and 0.5 mol % biotinylated lipid vesicles was almost similar at around 59.2 $\pm$ 1.5 and 58.3 $\pm$ 1.8 nm, respectively, while the height appreciably decreased to 51.5 $\pm$ 2.8 nm when the biotin ligand density was increased to 1 mol %. In contrast, at pH 4.5, the height decreased appreciably from 60.4 $\pm$ 3.0 to 54.1 $\pm$ 1.2 nm as the biotin fraction in the vesicle became higher from 0.25 to 0.5 mol % in line with the other trends discussed above, while the vesicles with 1 mol % biotin fraction retained a similar deformation extent, as indicated by a vesicle height around 56.2 $\pm$ 2.7 nm.

Based on the calculated basement radius values, we further estimated the area that contacts the SLB surface, $A = \pi r^2$, in different pH conditions as a function of biotinylated lipid fraction in the vesicles (Figure 4D). For the vesicle adlayer formed at pH 7.5, the contact area increased from 2478 $\pm$ 213 to 3099 $\pm$ 209 nm^2 when the molar fraction of biotinylated lipid ligand in the vesicles increased from 0.25 to 0.5 mol %, while the contact area became greater at 1 mol % biotin fraction, with a value of 4138 $\pm$ 200 nm^2. On the other hand, the contact area modestly increased at pH 6 to be 3321 $\pm$ 281, 3486 $\pm$ 340, and 4657 $\pm$ 458 nm^2 for 0.25, 0.5, and 1 mol % biotinylated lipid vesicles, respectively. Accordingly, for the

vesicle adlayer at pH 4.5, the corresponding contact area appreciably increased from 3094 ± 566 to 4245 ± 198 nm² in the range of 0.25−0.5 mol % biotin fraction in the vesicles and decreased to 3865 ± 481 nm² for the 1 mol % biotin fraction case. Collectively, the analytical calculation results further support that multivalency-induced vesicle shape deformation became more appreciable at lower ligand densities in pH 4.5 conditions than in pH 6 or 7.5 conditions.

Since the binding strength of the biotin−streptavidin interaction is similarly high across the tested range of pH conditions, the effects of solution pH on multivalency-induced vesicle shape deformation are related to pH-related changes in the membrane properties of vesicles rather than due to changes in the multivalent binding energy per biotin−streptavidin pair.[41,42] Indeed, past results indicate that the biotin−streptavidin binding interaction is mainly mediated by the van der Waals force along with extensive hydrogen bonding rather than by electrostatic forces[42,43] (see also Table S1 for typical pK_a values of amino acid side chains involved in the hydrogen bonds). It should also be noted that the effect of solution pH itself on the absolute extent of vesicle deformation is somewhat modest, which is consistent with the tendency for flat PC lipid bilayers to have similar levels of membrane bending rigidity scale-wise in various pH conditions.[27] It should be emphasized that the main observed pH-dependent effect relates to the extent to which the membrane bending energy counterposes the multivalent binding energy, which is the physical basis for driving vesicle shape deformation and was highly sensitive to the specific pH condition.

Quantification of Vesicle Surface Coverage. Using expression (1) for the LSPR signal, we also further characterized the vesicle adlayer properties near saturation (or, more specifically, at t = 65 min in Figure 2A−C), which allows us to obtain the surface concentration and the corresponding surface coverage of attached vesicles in different pH conditions and under varying degrees of multivalent binding interactions. This is possible provided the vesicle geometrical dimensions, R_v and r, are known. In this context, one should bear in mind that in general the vesicle−SLB contact area, πr^2, depends on the number of the ligand−receptor bonds there and can decrease with increasing vesicle surface concentration due to exhaustion of free receptors in the SLB. In addition, the vesicle geometry can change with increasing this concentration due to vesicle deformation related to vesicle−vesicle interactions. Our estimates indicate that in our case both of these factors are negligible (Section 2 in the Supporting Information), and accordingly we can use the R_v and r values obtained in the low-coverage limit to also describe the situation at saturation.

Figure 5 presents a summary of the calculation results, which display the surface concentration of attached vesicles, C_a, and the corresponding surface coverage, θ, that relate to how much of the SLB surface is covered by attached vesicles. The vesicle surface concentration at pH 7.5 were around 58 ± 2, 65 ± 2, and 56 ± 1 μm^{-2} for the vesicles with 0.25, 0.5, and 1 mol % biotinylated lipid, respectively. At pH 6, the corresponding surface concentration was determined to be around 52 ± 4, 61 ± 3, and 53 ± 2 μm^{-2} when the mol % of biotin ligand in the vesicles increased from 0.25 to 1 mol %, while the corresponding values were around 57 ± 5, 57 ± 2, and 60 ± 4 μm^{-2} at pH 4.5. While the differences in the surface concentration of attached vesicles are rather small in terms of ligand density and solution pH, we may add a few remarks
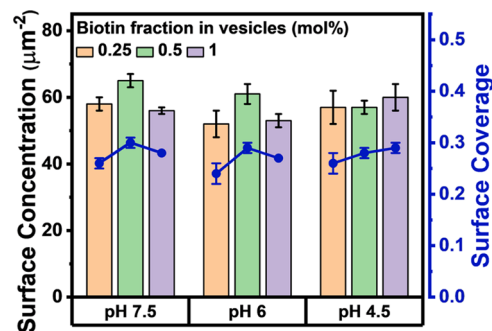
Figure 5. Molecular quantification of vesicle packing at saturation on the SLB surface. Surface concentration and the corresponding surface coverage (blue circles with lines for visualization) of attached vesicles on the SLB platform as a function of biotinylated lipid ligand fraction in the vesicles at each pH condition. All measurement values are presented as the mean ± standard deviation from n = 3 experiments.

regarding tendencies. In the pH 7.5 case, the surface concentration values significantly increased from 0.25 to 0.5 mol % fractions and then significantly decreased again at 1 mol % fraction (P < 0.05, one-way ANOVA). This result supports that initially increasing the ligand density from 0.25 to 0.5 mol % modestly enhances shape deformation of attached vesicles to increase the total surface concentration (i.e., greater surface coverage per vesicle) while further increasing the ligand density to 1 mol % causes appreciable vesicle shape deformation to assume nonspherical geometries that affect vesicle−vesicle packing interactions and vesicle surface concentration at saturation accordingly. Similar results were also obtained at pH 6. By contrast, appreciable vesicle shape deformation in the pH 4.5 case already occurred at 0.5 mol % fraction so the surface concentration of attached vesicles remained similar across the tested ligand densities in that case.

The corresponding surface coverage of vesicles on the SLB surface, θ, was also calculated by $\pi R_v^2 C_a$. For the vesicle adlayers at pH 7.5, the surface coverage at saturation was determined to be around 0.26 ± 0.01 when the biotinylated lipid fraction in the vesicles was 0.25 mol %, while the value increased to around 0.30 ± 0.01 and ∼0.28 for 0.5 and 1 mol % biotinylated lipid vesicles, respectively. Similarly, the corresponding surface coverage of the vesicle adlayers at pH 6 was 0.24 ± 0.02 for 0.25 mol % biotinylated lipid vesicle and 0.29 ± 0.01 and ∼0.27 for 0.5 and 1 mol % biotinylated lipid vesicles, respectively, and those at pH 4.5 were 0.26 ± 0.02, 0.28 ± 0.01, and 0.29 ± 0.01 when the biotinylated lipid fractions in the vesicles were 0.25, 0.5, and 1 mol %, respectively. Compared to the jamming limit of nondeformed, spherical vesicles (determined to be ∼0.54 based on the random sequential adsorption model[44]), these values indicate that multivalency-induced vesicle shape deformation translates into smaller jamming limits that arise from the nonspherical geometry of the attached vesicles. Indeed, when attached vesicles undergo greater shape deformation, they adopt a more ellipsoidal-like shape, and thus, the vesicles are less efficiently packed on the SLB surface while the absolute effect magnitude-wise is relatively minor.

■ CONCLUSIONS

Using the LSPR sensing technique, we monitored the multivalent binding interactions of ligand-modified lipid vesicles with a receptor-modified SLB platform across a

range of biologically relevant pH conditions. Our experimental approach focused on varying the magnitude of the multivalent binding energy by adjusting the ligand density in the vesicles, and we observed that the solution pH affected sensitivity to multivalency-induced shape deformation of attached vesicles, with greater sensitivity at pH 4.5 than at pH 6 and 7.5. Specifically, appreciable vesicle deformation occurs when the multivalent binding energy (varied according to the ligand density) becomes appreciably larger than the opposing membrane bending energy and the corresponding transition point was around 0.5 mol % ligand fraction (weaker multivalency) at pH 4.5 and around 1 mol % ligand fraction (stronger multivalency) at pH 6 and 7.5. Hence, while high-curvature lipid membranes are known to generally have high membrane bending energy in all cases, these results reveal the subtle yet significant pH-related differences in the sensitivity to which ligand-modified lipid vesicles undergo shape deformation in response to multivalent binding interactions at lipid membrane interfaces.

Our experiments were conducted with zwitterionic PC lipids as the main vesicle component because they are widely utilized in liposomal nanomedicine compositions and as helper lipids in LNP formulations,[45] while the bioanalytical measurement capabilities in this study can be further extended to study various lipid classes, especially ionizable lipids that exhibit pH-dependent behavior.[12] At present, lipid engineering development platforms have mainly focused on biological or biological-mimicking assays[46,47] and a stronger emphasis on membrane biophysics may enhance scientific knowledge while also laying the groundwork to design functional lipids with tailored biophysical properties. In addition to liposomal drug delivery systems and other LNP technologies, these measurement capabilities have broad potential to be applied to study various biological nanoparticle systems such as membrane-enveloped virus particles and cancer exosomes, especially in contexts related to multivalent ligand−receptor interactions at lipid membrane interfaces.

ASSOCIATED CONTENT

Supporting Information

The Supporting Information is available free of charge at https://pubs.acs.org/doi/10.1021/acs.langmuir.3c00777.

Summary of side-chain pK_a values of streptavidin amino acids involved in hydrogen-bonding interactions with biotin (Table S1); summary of attached vesicle deformation analysis (Table S2); summary of calculation results for vesicle adlayer quantification (Table S3); and additional LSPR characterization data (Figure S1) (PDF)

AUTHOR INFORMATION

Corresponding Authors

Nam-Joon Cho − School of Materials Science and Engineering, Nanyang Technological University, 637553, Singapore; orcid.org/0000-0002-8692-8955; Email: njcho@ntu.edu.sg

Joshua A. Jackman − School of Chemical Engineering, Sungkyunkwan University, Suwon 16419, Republic of Korea; Translational Nanobioscience Research Center, Sungkyunkwan University, Suwon 16419, Republic of Korea; orcid.org/0000-0002-1800-8102; Email: jjackman@skku.edu

Authors

Hyeonjin Park − School of Chemical Engineering, Sungkyunkwan University, Suwon 16419, Republic of Korea; Translational Nanobioscience Research Center, Sungkyunkwan University, Suwon 16419, Republic of Korea; School of Materials Science and Engineering, Nanyang Technological University, 637553, Singapore

Tun Naw Sut − School of Chemical Engineering, Sungkyunkwan University, Suwon 16419, Republic of Korea; Translational Nanobioscience Research Center, Sungkyunkwan University, Suwon 16419, Republic of Korea

Abdul Rahim Ferhan − School of Materials Science and Engineering, Nanyang Technological University, 637553, Singapore; orcid.org/0000-0003-3238-3125

Bo Kyeong Yoon − School of Healthcare and Biomedical Engineering, Chonnam National University, Yeosu 59626, Republic of Korea

Vladimir P. Zhdanov − Division of Nano and Biophysics, Department of Physics, Chalmers University of Technology, Gothenburg 41296, Sweden; Boreskov Institute of Catalysis, Russian Academy of Sciences, Novosibirsk 630090, Russia; orcid.org/0000-0002-0167-8783

Complete contact information is available at:
https://pubs.acs.org/10.1021/acs.langmuir.3c00777

Notes
The authors declare no competing financial interest.

REFERENCES

(1) Gonda, A.; Kabagwira, J.; Senthil, G. N.; Wall, N. R. Internalization of Exosomes through Receptor-Mediated Endocytosis. Mol. Cancer Res. 2019, 17, 337−347.
(2) Cuellar-Camacho, J. L.; Bhatia, S.; Reiter-Scherer, V.; Lauster, D.; Liese, S.; Rabe, J. P.; Herrmann, A.; Haag, R. Quantification of Multivalent Interactions between Sialic Acid and Influenza A Virus Spike Proteins by Single-Molecule Force Spectroscopy. J. Am. Chem. Soc. 2020, 142, 12181−12192.
(3) Mammen, M.; Choi, S. K.; Whitesides, G. M. Polyvalent Interactions in Biological Systems: Implications for Design and Use of Multivalent Ligands and Inhibitors. Angew. Chem., Int. Ed. 1998, 37, 2754−2794.
(4) Mitchell, M. J.; Billingsley, M. M.; Haley, R. M.; Wechsler, M. E.; Peppas, N. A.; Langer, R. Engineering Precision Nanoparticles for Drug Delivery. Nat. Rev. Drug Discovery 2021, 20, 101−124.
(5) Ginini, L.; Billan, S.; Fridman, E.; Gil, Z. Insight into Extracellular Vesicle-Cell Communication: From Cell Recognition to Intracellular Fate. Cells 2022, 11, 1375.

(6) Overeem, N. J.; van der Vries, E.; Huskens, J. A Dynamic, Supramolecular View on the Multivalent Interaction between Influenza Virus and Host Cell. *Small* **2021**, *17*, 2007214.

(7) Kou, L.; Bhutia, Y. D.; Yao, Q.; He, Z.; Sun, J.; Ganapathy, V. Transporter-Guided Delivery of Nanoparticles to Improve Drug Permeation across Cellular Barriers and Drug Exposure to Selective Cell Types. *Front. Pharmacol.* **2018**, *9*, 27.

(8) Stamou, D.; Duschl, C.; Delamarche, E.; Vogel, H. Self-Assembled Microarrays of Attoliter Molecular Vessels. *Angew. Chem., Int. Ed.* **2003**, *42*, 5580−5583.

(9) Yoshina-Ishii, C.; Miller, G. P.; Kraft, M. L.; Kool, E. T.; Boxer, S. G. General Method for Modification of Liposomes for Encoded Assembly on Supported Bilayers. *J. Am. Chem. Soc.* **2005**, *127*, 1356−1357.

(10) Almeida-Marrero, V.; Bethlehem, F.; Longo, S.; Bertolino, M. C.; Torres, T.; Huskens, J.; de la Escosura, A. Tailored Multivalent Targeting of Siglecs with Photosensitizing Liposome Nanocarriers. *Angew. Chem., Int. Ed.* **2022**, *61*, e202206900.

(11) Williams, T. L.; Vareiro, M. M.; Jenkins, A. T. A. Fluorophore-Encapsulated Solid-Supported Bilayer Vesicles: A Method for Studying Membrane Permeation Processes. *Langmuir* **2006**, *22*, 6473−6476.

(12) Aliakbarinodehi, N.; Gallud, A.; Mapar, M.; Wesén, E.; Heydari, S.; Jing, Y.; Emilsson, G.; Liu, K.; Sabirsh, A.; Zhdanov, V. P.; Lindfors, L.; Esbjörner, E. K.; Höök, F. Interaction Kinetics of Individual mRNA-Containing Lipid Nanoparticles with an Endosomal Membrane Mimic: Dependence on pH, Protein Corona Formation, and Lipoprotein Depletion. *ACS Nano* **2022**, *16*, 20163−20173.

(13) Di Iorio, D.; Lu, Y.; Meulman, J.; Huskens, J. Recruitment of Receptors at Supported Lipid Bilayers Promoted by the Multivalent Binding of Ligand-Modified Unilamellar Vesicles. *Chem. Sci.* **2020**, *11*, 3307−3315.

(14) Block, S.; Zhdanov, V. P.; Höök, F. Quantification of Multivalent Interactions by Tracking Single Biological Nanoparticle Mobility on a Lipid Membrane. *Nano Lett.* **2016**, *16*, 4382−4390.

(15) Park, H.; Sut, T. N.; Yoon, B. K.; Zhdanov, V. P.; Cho, N.-J.; Jackman, J. A. Unraveling How Multivalency Triggers Shape Deformation of Sub-100 nm Lipid Vesicles. *J. Phys. Chem. Lett.* **2021**, *12*, 6722−6729.

(16) Hoshyar, N.; Gray, S.; Han, H.; Bao, G. The Effect of Nanoparticle Size on In Vivo Pharmacokinetics and Cellular Interaction. *Nanomedicine* **2016**, *11*, 673−692.

(17) Park, H.; Sut, T. N.; Yoon, B. K.; Zhdanov, V. P.; Kim, J. W.; Cho, N.-J.; Jackman, J. A. Multivalency-Induced Shape Deformation of Nanoscale Lipid Vesicles: Size-Dependent Membrane Bending Effects. *J. Phys. Chem. Lett.* **2022**, *13*, 1480−1488.

(18) Norling, K.; Sjöberg, M.; Bally, M.; Zhdanov, V. P.; Parveen, N.; Höök, F. Dissimilar Deformation of Fluid-and Gel-Phase Liposomes Upon Multivalent Interaction with Cell Membrane Mimics Revealed Using Dual-Wavelength Surface Plasmon Resonance. *Langmuir* **2022**, *38*, 2550−2560.

(19) Rosigkeit, S.; Meng, M.; Grunwitz, C.; Gomes, P.; Kreft, A.; Hayduk, N.; Heck, R.; Pickert, G.; Ziegler, K.; Abassi, Y.; et al. Monitoring Translation Activity of mRNA-Loaded Nanoparticles in Mice. *Mol. Pharmaceutics* **2018**, *15*, 3909−3919.

(20) Park, H.; Sut, T. N.; Yoon, B. K.; Zhdanov, V. P.; Cho, N.-J.; Jackman, J. A. Unraveling How Cholesterol Affects Multivalency-Induced Membrane Deformation of Sub-100 nm Lipid Vesicles. *Langmuir* **2022**, *38*, 15950−15959.

(21) Zhou, Y.; Raphael, R. M. Effect of Salicylate on the Elasticity, Bending Stiffness, and Strength of SOPC Membranes. *Biophys. J.* **2005**, *89*, 1789−1801.

(22) Buschmann, M. D.; Carrasco, M. J.; Alishetty, S.; Paige, M.; Alameh, M. G.; Weissman, D. Nanomaterial Delivery Systems for mRNA Vaccines. *Vaccines* **2021**, *9*, 65.

(23) Hou, X.; Zaks, T.; Langer, R.; Dong, Y. Lipid Nanoparticles for mRNA Delivery. *Nat. Rev. Mater.* **2021**, *6*, 1078−1094.

(24) Hajj, K. A.; Whitehead, K. A. Tools for Translation: Non-Viral Materials for Therapeutic mRNA Delivery. *Nat. Rev. Mater.* **2017**, *2*, 17056.

(25) Huotari, J.; Helenius, A. Endosome Maturation. *EMBO J.* **2011**, *30*, 3481−3500.

(26) Zhou, Y.; Raphael, R. M. Solution pH Alters Mechanical and Electrical Properties of Phosphatidylcholine Membranes: Relation between Interfacial Electrostatics, Intramembrane Potential, and Bending Elasticity. *Biophys. J.* **2007**, *92*, 2451−2462.

(27) Boggara, M. B.; Faraone, A.; Krishnamoorti, R. Effect of pH and Ibuprofen on the Phospholipid Bilayer Bending Modulus. *J. Phys. Chem. B* **2010**, *114*, 8061−8066.

(28) Petelska, A. D.; Figaszewski, Z. A. Effect of pH on the Interfacial Tension of Lipid Bilayer Membrane. *Biophys. J.* **2000**, *78*, 812−817.

(29) Zimmermann, R.; Küttner, D.; Renner, L.; Kaufmann, M.; Zitzmann, J.; Müller, M.; Werner, C. Charging and Structure of Zwitterionic Supported Bilayer Lipid Membranes Studied by Streaming Current Measurements, Fluorescence Microscopy, and Attenuated Total Reflection Fourier Transform Infrared Spectroscopy. *Biointerphases* **2009**, *4*, 1−6.

(30) Akimov, S. A.; Polynkin, M. A.; Jiménez-Munguía, I.; Pavlov, K. V.; Batishchev, O. V. Phosphatidylcholine Membrane Fusion Is pH-Dependent. *Int. J. Mol. Sci.* **2018**, *19*, 1358.

(31) Marsh, D. *Handbook of Lipid Bilayers*; CRC Press: Boca Raton, London, NY, 1990.

(32) Kolahdouzan, K.; Jackman, J. A.; Yoon, B. K.; Kim, M. C.; Johal, M. S.; Cho, N.-J. Optimizing the Formation of Supported Lipid Bilayers from Bicellar Mixtures. *Langmuir* **2017**, *33*, 5052−5064.

(33) Jackman, J. A.; Cho, N.-J. Supported Lipid Bilayer Formation: Beyond Vesicle Fusion. *Langmuir* **2020**, *36*, 1387−1400.

(34) MacDonald, R. C.; MacDonald, R. I.; Menco, B. P. M.; Takeshita, K.; Subbarao, N. K.; Hu, L.-r. Small-Volume Extrusion Apparatus for Preparation of Large, Unilamellar Vesicles. *Biochim. Biophys. Acta, Biomembr.* **1991**, *1061*, 297−303.

(35) Di Iorio, D.; Verheijden, M. L.; van der Vries, E.; Jonkheijm, P.; Huskens, J. Weak Multivalent Binding of Influenza Hemagglutinin Nanoparticles at a Sialoglycan-Functionalized Supported Lipid Bilayer. *ACS Nano* **2019**, *13*, 3413−3423.

(36) Fredriksson, H.; Alaverdyan, Y.; Dmitriev, A.; Langhammer, C.; Sutherland, D. S.; Zäch, M.; Kasemo, B. Hole−Mask Colloidal Lithography. *Adv. Mater.* **2007**, *19*, 4297−4302.

(37) Langhammer, C.; Larsson, E. M.; Kasemo, B.; Zorić, I. Indirect Nanoplasmonic Sensing: Ultrasensitive Experimental Platform for Nanomaterials Science and Optical Nanocalorimetry. *Nano Lett.* **2010**, *10*, 3529−3538.

(38) Dahlin, A. B.; Tegenfeldt, J. O.; Höök, F. Improving the Instrumental Resolution of Sensors Based on Localized Surface Plasmon Resonance. *Anal. Chem.* **2006**, *78*, 4416−4423.

(39) Jackman, J. A.; Zhdanov, V. P.; Cho, N.-J. Nanoplasmonic Biosensing for Soft Matter Adsorption: Kinetics of Lipid Vesicle Attachment and Shape Deformation. *Langmuir* **2014**, *30*, 9494−9503.

(40) Jackman, J. A.; Yorulmaz Avsar, S.; Ferhan, A. R.; Li, D.; Park, J. H.; Zhdanov, V. P.; Cho, N.-J. Quantitative Profiling of Nanoscale Liposome Deformation by a Localized Surface Plasmon Resonance Sensor. *Anal. Chem.* **2017**, *89*, 1102−1109.

(41) Sut, T. N.; Park, H.; Koo, D. J.; Yoon, B. K.; Jackman, J. A. Distinct Binding Properties of Neutravidin and Streptavidin Proteins to Biotinylated Supported Lipid Bilayers: Implications for Sensor Functionalization. *Sensors* **2022**, *22*, 5185.

(42) Miyamoto, S.; Kollman, P. A. Absolute and Relative Binding Free Energy Calculations of the Interaction of Biotin and Its Analogs with Streptavidin Using Molecular Dynamics/Free Energy Perturbation Approaches. *Proteins: Struct., Funct., Bioinf.* **1993**, *16*, 226−245.

(43) Liu, F.; Zhang, J. Z.; Mei, Y. The Origin of the Cooperativity in the Streptavidin-Biotin System: A Computational Investigation through Molecular Dynamics Simulations. *Sci. Rep.* **2016**, *6*, 27190.

(44) Hinrichsen, E. L.; Feder, J.; Jøssang, T. Geometry of Random Sequential Adsorption. *J. Stat. Phys.* **1986**, *44*, 793−827.

(45) Hassett, K. J.; Benenato, K. E.; Jacquinet, E.; Lee, A.; Woods, A.; Yuzhakov, O.; Himansu, S.; Deterling, J.; Geilich, B. M.; Ketova, T.; et al. Optimization of Lipid Nanoparticles for Intramuscular Administration of mRNA Vaccines. *Mol. Ther. Nucleic Acids* **2019**, *15*, 1−11.

(46) Hassett, K. J.; Higgins, J.; Woods, A.; Levy, B.; Xia, Y.; Hsiao, C. J.; Acosta, E.; Almarsson, Ö.; Moore, M. J.; Brito, L. A. Impact of Lipid Nanoparticle Size on mRNA Vaccine Immunogenicity. *J. Controlled Release* **2021**, *335*, 237−246.

(47) Lee, S. M.; Cheng, Q.; Yu, X.; Liu, S.; Johnson, L. T.; Siegwart, D. J. A Systematic Study of Unsaturation in Lipid Nanoparticles Leads to Improved mRNA Transfection In Vivo. *Angew. Chem., Int. Ed.* **2021**, *60*, 5848−5853.